NANO · MICRO small
www.small-journal.com

Continuous Vat Photopolymerization for Optical Lens Fabrication

*Han Xu, Shuai Chen, Renzhi Hu, Muqun Hu, Yang Xu, Yeowon Yoon, and Yong Chen**

Optical lenses require feature resolution and surface roughness that are beyond most (3D) printing methods. A new continuous projection-based vat photopolymerization process is reported that can directly shape polymer materials into optical lenses with microscale dimensional accuracy (< 14.7 µm) and nanoscale surface roughness (< 20 nm) without post-processing. The main idea is to utilize frustum layer stacking, instead of the conventional 2.5D layer stacking, to eliminate staircase aliasing. A continuous change of mask images is achieved using a zooming-focused projection system to generate the desired frustum layer stacking with controlled slant angles. The dynamic control of image size, objective and imaging distances, and light intensity involved in the zooming-focused continuous vat photopolymerization are systematically investigated. The experimental results reveal the effectiveness of the proposed process. The 3D-printed optical lenses with various designs, including parabolic lenses, fisheye lenses, and a laser beam expander, are fabricated with a surface roughness of 3.4 nm without post-processing. The dimensional accuracy and optical performance of the 3D-printed compound parabolic concentrators and fisheye lenses within a few millimeters are investiagted. These results highlight the rapid and precise nature of this novel manufacturing process, demonstrating a promising avenue for future optical component and device fabrication.

1. Introduction

Additive manufacturing (AM), also known as 3D printing, fabricates 3D objects from a digital 3D model by accumulating material at designated locations.[1] Benefiting from rapid turnaround and high customizability, additive manufacturing has been widely used in dental, surgical, biomedical, and other applications.[2–10] Among all the AM processes, mask image projection-based vat photopolymerization (MIP-VPP) converts liquid monomers into solid polymers in a layer-by-layer manner using controlled UV light, achieving the micro-scale resolution and centimeter scale fabrication size. It has been a widely used AM process to fabricate parts with high accuracy and surface finish, which sheds light on direct printing optical lenses.[11–14] While the femtosecond laser direct-write-based two-photon polymerization (TPP) has been increasingly used in micro-optics fabrication,[15–17] the one-photon-based MIP-VPP to 3D print optical components is desired due to its significantly lower equipment cost and a much faster fabrication speed than TPP. [18] Many attempts to use MIP-VPP to 3D print optical components have been made.[19,20] However, most optical lenses with extremely high surface roughness requirements (≈10–500 nm) are still not 3D printable by one-photon vat polymerization.[21–23] MIP-VPP follows the schema of stacking 2.5D thin sheets layer-by-layer in fabricating 3D products. Laminar sheets generated from the sliced computer-aided design (CAD) model with specific layer thickness are converted into pixelated mask images and projected to the photocurable resin, as shown in **Figure 1**a-left. The curing results from a sliced layer is a 2.5D extrusion of the mask images from that layer, as shown in Figure 1a-right. The red curve in the magnified figure is the profile of designed CAD models, whereas the green area is the cured layers. The Intrinsic discontinuities in pixels and layers lead to the staircase stepping on the printed surface, which deteriorates 3D objects' surface quality. A critical barrier for AM to overcome is how to reduce pixel size and layer thickness to achieve the high resolution and surface roughness required by optical lenses.

Continuous liquid interface production (CLIP) developed by Carbon 3D offers a strategy to reduce the layer thickness to a submicron scale.[24] As Figure 1b-left shows, the CLIP process

H. Xu, S. Chen, R. Hu, Y. Xu, Y. Yoon, Y. Chen
Center for Advanced Manufacturing
University of Southern California
Los Angeles, CA 90007, USA
E-mail: yongchen@usc.edu
H. Xu, Y. Xu, Y. Chen
Daniel J. Epstein Department of Industrial and Systems Engineering
University of Southern California
Los Angeles, CA 90089, USA
S. Chen, R. Hu, M. Hu, Y. Yoon, Y. Chen
Department of Aerospace and Mechanical Engineering
University of Southern California
Los Angeles, CA 90089, USA

The ORCID identification number(s) for the author(s) of this article can be found under https://doi.org/10.1002/smll.202300517

DOI: 10.1002/smll.202300517

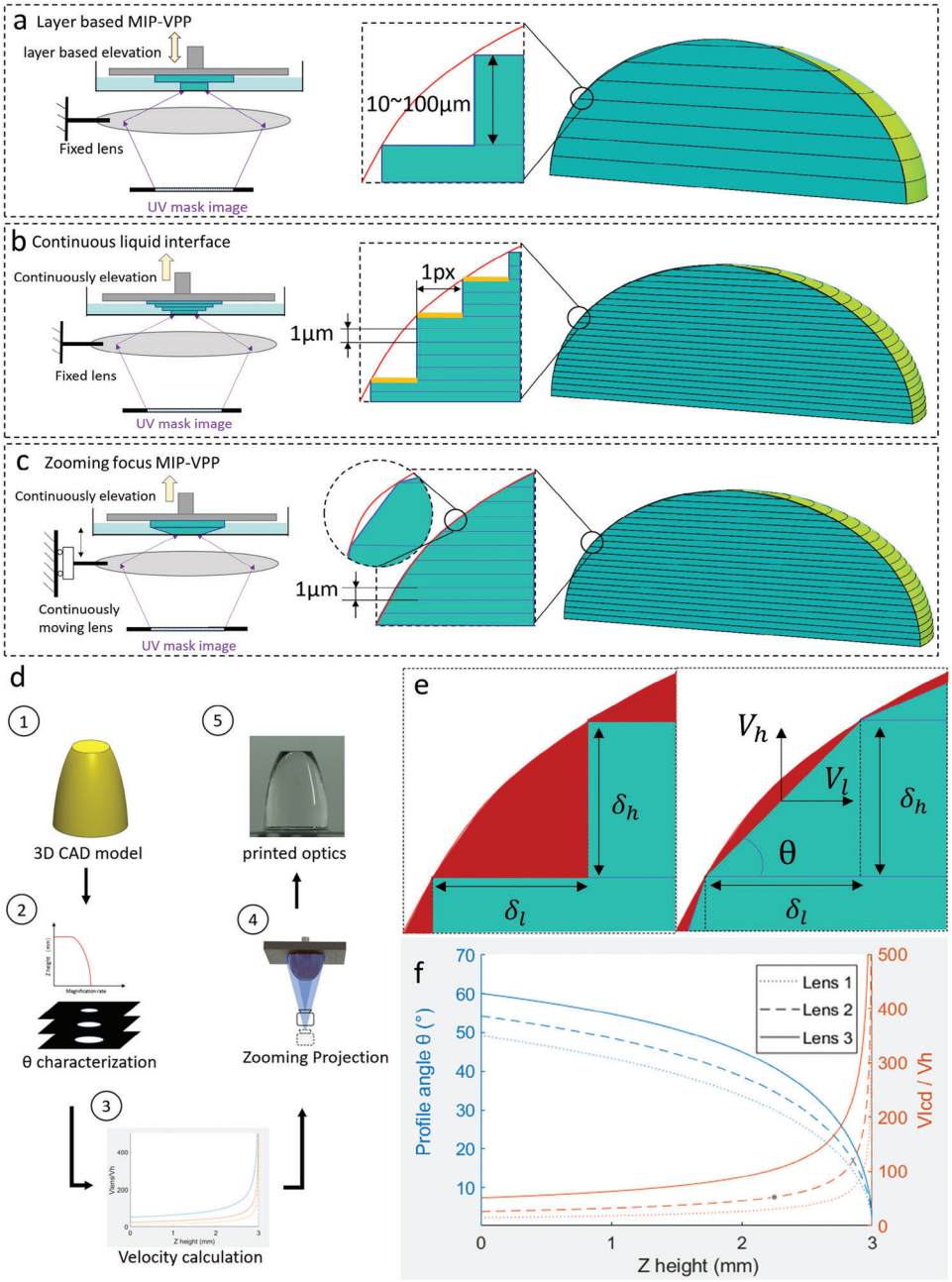

Figure 1. 3D printing of optical lenses using zooming-focused MIP-VPP. a–c) The comparison of the MIP-VPP processes and the resulting surface finish. a) Optical lenses printed by layer-based MIP-VPP. The staircase stepping is formed between layers. b) Optical lenses printed by continuous liquid interface production (CLIP). The pixel size limits the surface finish. c) Optical lenses printed by zooming-focused MIP-VPP and the frustum layer stacking. d) A schematic illustration of zooming-focused MIP-VPP. The process starts with CAD design, followed by profile characterization, velocity calculation, zooming-focused mask image projection, and final cleaning. e) The generation of the frustum layer stacking. The printed part is marked in green. The metric error of the layer stacking is marked in red. e)-left the metric error of 2.5D layer stacking. e)-right the metric error of the frustum layer stacking. f) The control of the slant angle over the *Z* height. The slant angle (blue curves) is determined by the moving velocity (orange curves) of the LCD mask and the building platform.

projects a high-framerate UV mask video onto the building platform while the building platform continuously elevates from the resin vat. The high framerate mask video enables the super slicing of the CAD model to less than 1 μm thin sheets, significantly reducing the staircase stepping. Based on this process, Chen et al. introduced a CLIP process combining grayscale exposure and meniscus coating that fabricates aspherical lenses with surface roughness down to 7 nm after meniscus coating.[25,26] Zhang et al. introduced a single droplet continuous MIP-VPP that uses the liquid film covering to fabricate contact eye lenses.[27] However,

while the layer thickness is significantly reduced in the CLIP processes, the change of mask images is still not smooth, mainly because the pixel size of a mask image defines the smallest projection light change, [28,29] as Figure 1b-right shows. As illustrated in yellow lines, the staircase stepping caused by the discrete change of mask images is at a one-pixel scale (at 10 μm level), which is still not smooth for optical lens fabrication. Thus, in the previous studies, the 3D-printed optical lenses need to be post-processed using meniscus coating or polishing to reach a good surface finish. In addition to reducing the manufacturing speed, post-processing often makes dimensional accuracy uncontrollable.[30–32]

A zooming-focused MIP-VPP is developed as a dimensionally accurate and time-efficient strategy to circumvent the critical issues for optical lens fabrication. The proposed process utilizes a moving objective lens to dynamically change the projection images while continuously elevating the building platform (Figure 1c-left). This configuration enables the frustum layer stacking with controlled layer tilting angles, as shown in Figure 1c-right. Unlike 2.5D layer stacking, each layer of the frustum layer stacking has a slope for its side surface (defined as a slant angle). Hence, the frustum layer stacking requires not only the information on the cross-sectional image but also the slant angle of the 3D model. As a result, the 3D-printed surfaces by the frustum layer stacking have three orders of magnitude smaller staircase stepping errors than those by the 2.5D layer stacking under the same layer thickness (Figure S8 and Table S1, Supporting Information). By combining frustum layer stacking and the super slicing technique from CLIP, the zooming-focused MIP-VPP improves the surface smoothness to less than ten nanometers, enabling the direct printing of optical lenses with a smooth surface roughness (with an average of 3.4 nm) and accurate dimension (less than 14.7 μm).

Here, we report a new strategy of 3D printing super-sliced frustum layers by continuously changing the mask images on the continuously elevating building platform for optical lens fabrication. To develop the zooming-focused MIP-VPP process, we first present essential parameters in terms of the fabrication scale, speed, and resolution, satisfying the requirements of optical lens fabrication. Next, the model of the light intensity distribution of the zooming-focused imaging system is systematically evaluated. This is followed by a model-based light intensity compensation to achieve uniform light intensity during fabrication as the focus changes. Finally, the test cases of compound parabolic concentrators, fisheye lenses, and a laser beam expander with customized sizes and shapes have been designed to demonstrate the dimensional accuracy, surface smoothness, and optical properties of this new AM process.

2. Results and Discussion

Zooming-focused MIP-VPP eliminates staircase stepping by employing a continuously changed mask image to build a frustum layer with a super-sliced layer thickness. Figure 1d shows the overview of zooming-focused MIP-VPP. 1) A 3D CAD model is designed based on the geometry of an optical lens. 2) The designed 3D CAD model is super sliced into a set of thin frustum layers whose slant angle θ and cross-sectional images are correspondingly characterized over the Z direction of the CAD model. 3) The motion planner converts the data of the slant angle θ into the moving velocity of the objective lens, the liquid crystal display (LCD) photomask, and the building platform. 4) A zooming-focused MIP-VPP apparatus builds the frustum layers in continuous printing. 5) After bathing and nitrogen flow cleaning, the printed optical lenses can achieve less than 3.4 nm surface roughness and micron-scale dimensional accuracy. The essence of this process is that the frustum layer stacking is applied to provide a close approximation in regenerating 3D models and to reduce the staircase stepping (Figure 1e-right). Note, in our method, the side surface of each frustum layer has the same slant angle θ. Hence it only applies to the symmetric shapes along the Z-axis. Fortunately, most optical lenses are symmetric along the optical axis.

A frustum layer of an optical lens is generated by following three steps: 1) the CAD model is sliced into a series of cross-sectional images under a certain layer thickness δ_h. 2) The difference between a cross-sectional image and its neighboring cross-sectional images is given by $\delta_l(k) = \frac{(l_k - l_{k-1})}{2}$, where l_k is the characteristic length of the k_{th} layer cross-section image. 3) Based on the k_{th} and the $(k-1)_{th}$ cross-sectional images, a frustum layer can be constructed as a linear interpolation of its neighbors, whose slope angle θ of the side surface is defined as $tan\theta = \delta_h/\delta_l$. To evaluate different layer stackings' performance, we use an intermediate metric profile in the previous work to quantify the approximation error of a CAD model.[33] The layer stacking approximation errors by the 2.5D and frustum layer stackings under the same layer thickness δ_h are demonstrated in Figure 1e, shown as the red color for both layer stacking methods. In Figure 1e-left, the 2.5D layer stackings marked in green have vertical staircase stepping for each layer. The 2.5D layer stacking omits the geometric information between two cross-sectional images in the approximation, leading to a noticeable missing error for optical lenses. In comparison, the frustum layer stacking (Figure 1e-right) considers both the cross-sectional images and the corresponding slant angle of the side surface of each layer, leading to a volumetric error ϵ_k that is three orders smaller (Figure S8 and Table S1, Supporting Information).

To physically enable the frustum layer stacking in MIP-VPP, we continuously adjust the size of the mask images during the printing process. That is, the printing of a frustum layer with a certain slant angle θ can be achieved by controlling V_h and V_l, where V_l is the changing speed of the projection images and V_h is the part printing speed in the Z direction (Figure 1e-left). V_l is further determined by the velocity of the LCD V_{lcd}, focal length, the diameter of the mask images on the LCD screen, and the distance between the objective lens and the building platform (refer to Method S1, Supporting Information). Thus, the slant angle θ is governed by the following equation.

$$tan(\theta) = \frac{V_h}{V_l} = \frac{-2V_h\left(d_o - f\right)^2}{V_{lcd} f D} \tag{1}$$

where f is the focal length of the objective lens, D is the diameter of the mask images, and d_o is the distance between the objective lens and the building platform. In this case, the designated slant angle θ of the frustum layer can be achieved by manipulating the velocity of the LCD photomask V_{lcd} and the printing speed

V_h. An example of motion planning to generate the desired frustum layer stacking of different optical lenses is demonstrated in Figure 1f. The CAD models of three different parabolic lenses are converted into slant angles θ over the Z height shown in the blue curve. Based on the slant angle θ, the velocity ratio V_{lcd}/V_h over the Z height calculated using Equation (1) is plotted in Figure 1f in orange. The value of V_{lcd}/V_h increases as the Z height increases from 0 to 3 mm since the profile slant angle θ decreases. At the very tip of the parabolic lens, V_{lcd}/V_h will reach its maximum to fabricate a nearly flat frustum layer. The printing speed V_h is related to light intensity and the curing depth of photocurable resin, which will be discussed in later sections.

To verify our idea, an in-house developed zooming-focused MIP-VPP apparatus was built, comprising a computer for the process planning, a microcontroller for the motion control, a 405 nm UV light emitting diode (LED), an objective lens movable in Z, an LCD mask movable in Z, a glass building platform, and a resin vat coated with polydimethylsiloxane (PDMS). (Figure S1, Supporting Information) The apparatus is configured in the bottom-up configuration.[34,35] The UV radiation emitted from the LED array shoots through the LCD photomask and is projected by the objective lens to the building platform. A light homogenizer is attached to the bottom of the LCD photomask to convert parallel UV light into diffuse light to generate uniform light intensity distribution. The objective lens and the LCD photomask are mounted on high-resolution Z linear stages that are separately controlled to adjust the objective and imaging distances during printing. The oxygen embedded in the PDMS membrane inhibits the free radical polymerization reactions, creating a non-photocurable dead zone near the membrane to prevent adhesion while simultaneously facilitating a sustained supply of fresh resin as the 3D-printed part is pulled up vertically in a continuous motion.[36,37] **Figure 2**a–c demonstrate the printing of a frustum layer via zooming-focused MIP-VPP. Figure 2a shows the magnified profile of a designed optical lens sliced into a frustum layer. Points 1 and 2, marked in yellow, are the bottom and the top of the frustum layer. The thickness of the frustum layer δ_h is 1 μm, and the slant angle is θ. The distance of the micro-steps λ is the theoretical resolution determined by the linear stage and focal length. Figure 2b,c shows the motions of the LCD photomask, the objective lens, and the building platform from point 1 to point 2. The objective lens starts at the position d_{i1} and the LCD photomask starts at position d_{o1}. During the continuous printing, the objective lens moves up at a velocity V_{lens} and the LCD photomask moves down at a velocity V_{lcd} to form the slant angle θ of the frustum layer at each time moment. The objective lens ends at position d_{i2} and the LCD photomask ends at the position d_{o2} to finish this frustum layer. As Figure 2a shows, a series of mask images with micro-step changes can be achieved on the building platform (marked in black). The size of projected mask images for micro-steps can be controlled by d_o and d_i, governed by the equation.

$$M = \frac{d_i}{d_o} \tag{2}$$

where M is the magnification rate of the mask images. Moreover, d_o and d_i are controlled by two linear stages that have a submicron resolution. Hence, this magnification rate control can break MIP-VPP's pixel size limitation in the XY resolution, enabling a projection image to continuously change its size and, consequently, define a frustum layer in the frustum layer stacking.

We demonstrate the physical mask images projected on the building platform during the printing process in Figure 2d. The mask images of a pyramid CAD model sliced from bottom to top are shown from A to E. Accordingly, the XY sizes of the mask images decrease from 1000 to 210 μm. The images at the bottom show a zoom-in view of the patterns whose XY sizes are between 600 to 590 μm, and their corresponding imaging distance d_i = 21.60 mm and d_i' = 21.54 mm. Hence, a linear stage actuated by a stepper motor with 0.5 μm resolution would provide 120 controllable steps between d_i and d_i', enabling the accurate control of the projection images with an achievable 83 nm XY change for the same mask image. This nanoscale XY resolution control of the projection images can achieve the continuous change of the projection light on the curing surface, enabling the printing of tilting side surfaces with a controlled slant angle θ during the frustum layer stacking.

The fabrication scale, resolution, and speed characterize the essential performance of zooming-focused MIP-VPP. Here we define the fabrication scale of zooming-focused MIP-VPP as the range of magnification rate since it is a multi-scale fabrication process where the fabrication size changes with the magnification rate. Figure 2e shows the change of M over d_o and d_i at three different focal lengths:f = 7.8, 18, and 28.9 mm. The red curve shows the objective distance d_o increases as the magnification rate decreases. The maximum of d_o limited by the length of the linear stage is from 0 mm to 380 mm. The maximum of d_i limited by the hardware is from 0 to 24.5 mm. The black lines show the imaging distance decreases as the magnification rate increases. The red lines show the objective distance increases as the magnification rate increases. The objective lens with a large focal length (f = 28.9 mm) cannot project a focused image at any magnification rate. An objective lens with a small focal length (f = 7.8 mm) provides a larger range of magnification rate. However, it has a narrower depth of field, making the accurate focus of the mask image difficult. (refer to Table S5, Supporting Information) Here, we select $f = 18mm$ in our prototype to balance the fabrication scale and the focus accuracy. The magnification rate within the working range derived from the hardware limits is $M = \approx 0.06$–0.35 (refer to Method S2, Supporting Information).

Besides the fabrication scale, the printing resolution is another essential parameter. The theoretical resolution λ of zooming-focused MIP-VPP is defined by the smallest controllable micro-steps of mask images on the building platform. It worsens as the focal length of the objective lens reduces and gets better as the focal length increases, as shown in Figure 2f since the smaller focal length makes the mask images more sensitive to d_o and d_i. Besides, the size of the mask images also determines the theoretical resolution. Here, the size of mask images in 1.5, 3, and 6 mm are plotted in blue, black, and red, respectively. The resolution of mask images increases as the size of the mask image decreases since the smaller mask image leads to a smaller mask image change for a one-step change in magnification rate. Finer resolution can be achieved using an imaging system with a longer focal length and a smaller mask image. However, as discussed previously, longer focal lengths lead to a smaller fabrication scale.

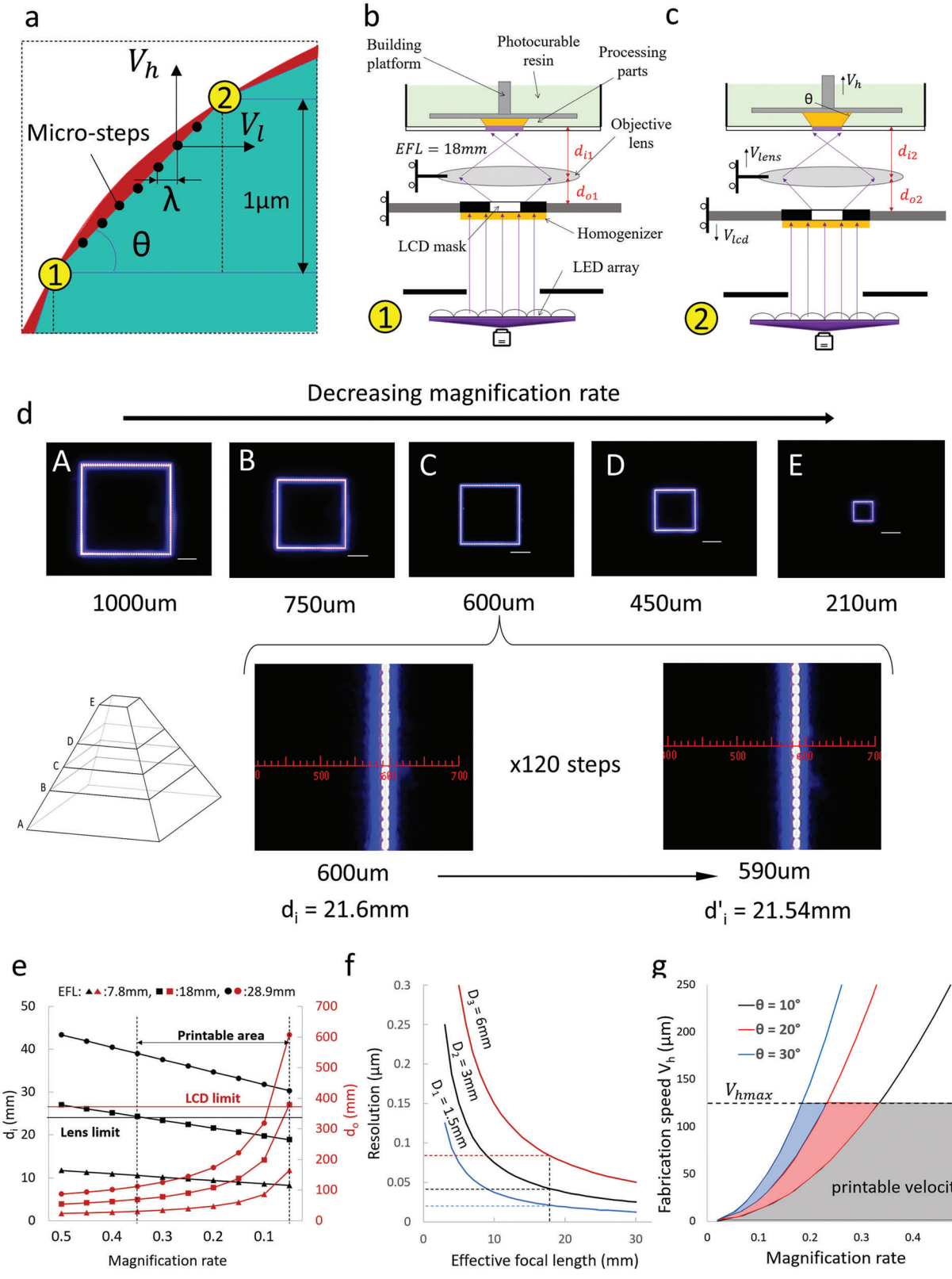

Figure 2. The mechanism of the zooming-focused MIP-VPP. a–c) The schematic plot of zooming-focused MIP-VPP to fabricate a frustum layer. a) The profile of the designed optics and a printed frustum layer. b) The components of a zooming-focused MIP-VPP system. The position of the objective lens, the LCD photomask, and the building platform when printing at point 1. c) The motions of the objective lens, the LCD photomask, and the building platform to generate the frustum layer. The position of the objective lens, the LCD photomask, and the building platform when printing at point 2. d) The

In our experiment, $f = 18mm$ and $D = 3mm$ were used in fabricating optical lenses, resulting in the theoretical resolution λ of 42 nm on the zooming size change of the mask images (refer to Method S3, Supporting Information).

Thirdly, the fabrication speed is limited by the polymerization speed V_{hmax} and the moving speed of the LCD photomask V_{lens}. The polymerization speed is set at $V_{hmax} = 120$ μm s^{-1} for good quality continuous liquid interface production.[38] The maximum speed of the linear stage of the LCD photomask is $V_{icdmax} = 22.8$ mm s^{-1}. Figure 2g shows the maximum printing speed over the magnification rate M, and the slant angle θ. The shaded area is the printable speed over the magnification rate. The maximum printing speed presents an increment as the magnification rate increase. Besides, as the slant angle increases, the maximum printing speed increases. In our working range, the fastest printing speed is $V_h = 5.4$ μm s^{-1} at $\theta = 10°$, $V_h = 10.8$ μm s^{-1} at $\theta = 20°$, and $V_h = 16.2$ μm s^{-1} at $\theta = 30°$, which is acceptable for high-resolution feature fabrication. The average printing speed is around 11.5 μm s^{-1} for most of the test cases (Table S4, Supporting Information). When it prints at a large magnification rate, the printing speed is determined by the photopolymerization speed, $V_h = V_{hmax} = 120$ μm s^{-1}. A higher printing speed can be used to build large cross-sectional images, which improves the products' throughputs. (refer to Method S4, Supporting Information)

One noteworthy difference between zooming-focused MIP-VPP and other MIP-VPP processes is the light intensity control during printing, since the projection image size of zooming-focused MIP-VPP changes while remaining the same in other MIP-VPP processes. The light intensity affects the photopolymerization behavior of the liquid resin.[39] Zooming-focused MIP-VPP introduces a change of the light intensity during modifying magnification rate. The incident light shooting on the LCD mask is scattered into a hemisphere with the light intensity in the Gaussian distribution. The energy of the diffused light over the scattering angle α follows the Gaussian distribution (Figure S4, Supporting Information).

$$I(\alpha, i_0) = \frac{i_0}{\sqrt{2\pi}\sigma} exp\left(\frac{-\alpha^2}{2\sigma^2}\right) \quad (3)$$

where i_0 is the emitting light intensity in the normal direction, and α is the diffused angle. A light cone within the spherical angle Ω derived from integrating the acceptance angle over the from $[0, 2\pi]$, is the light collected by the objective lens (**Figure 3**a).[40] Assume all light collected by the objective lens will be projected to the building platform. The light intensity on the building platform is given by:

$$I_{out} = \frac{1}{M}\iint_{\Omega} I(\alpha, i_0)\, d\Omega = \frac{1}{M}\int_0^{2\pi} d\varphi \int_0^{\Theta(\varphi, d_o, x_0, R)} I(\alpha, i_0)\, d\theta \quad (4)$$

where Ω is the spherical angle of the accepted light cone, R is the radius of the objective lens, and f is the focal length of the objective lens. (refer to Method S5, supporting information) For specific hardware, the R, $f \wedge i_0$ are constant numbers. The output light intensity only depends on the magnification rate and the central distance: $I_{out} = I_{out}(M, x_0)$. Based on this model, the relative energy dosage distribution of the zooming-focused MIP-VPP system was simulated, as shown in Figure 3b,c. The simulation results show the relative energy dosage E/E_0 over the magnification rate M and the pixel position X, where E is the energy dose of mask images at the building platform and E_0 is the energy dose of the mask images at the LCD mask. The relative energy dosage increases as the pixel locating closer to the optical center. The relative energy dosage at the optical center is around 40% stronger than that on the boundary of the building platform. Besides, the relative energy dosage is stronger when the magnification rate M is smaller since a smaller M leads to the light flux from the LCD mask concentrating to a smaller region. Within the printing area of our prototype (8 mm circle in radius), $E/E_0$is varying from 1 to 1.9. The nearly two times UV dose variance leads to undesired curing results. Within a frustum layer, the resin in the center of the LCD mask will be over-cured, while the resin on the boundary will be under-cured. For different frustum layers, the resin will be over-cured in areas with small magnification rates and under-cured in areas with large magnification rates.

A light-intensity compensation method needs to be implemented to generate a uniform photopolymerization result. Figure 3c shows the relative energy dosage over the pixel position and the magnification rate, respectively. The relative energy dosage over the pixel position follows a similar pattern for all the magnification rates, indicating the possibility of decoupling the two related parameters. Therefore, a two-step light-intensity compensation method is described as follows.

1) In the first step, grayscale-based mask image compensation is applied to the LCD screen, [41] as Figure 3d simulates. The two leftmost figures show the mask images with and without grayscale values applied to LCD. The top figure is the binary mask image without grayscale compensation, while the bottom figure is the mask image with grayscale values used. The figures on the right show the relative energy dosage E/E_0 with or without grayscale over the magnification rate M from 0.34 to 0.07. The value of E/E_0 is larger in the mask center and smaller on the boundary for the binary mask image. As a comparison, E/E_0 of the whole building area is uniform by using a grayscale mask image. The physical test case of a chessboard is demonstrated in Figure 3e to verify the effectiveness of the grayscale-based light intensity compensation. The original mask images (shown in Figure 3e-top) lead to a nonuniform photopolymerization result. The printed results have a larger square in the center, whereas a smaller

physical mask images captured from the building platform during the zooming-focused MIP-VPP printing. The top row of (d) shows the mask image change from 1000 to 210 μm. Scale bars: 200 μm. The bottom row of (d) shows the small division between mask images. e) The influence of objective and imaging distances on the magnification rate. The horizontal lines in red and black show the hardware limit of objective and imaging distances, respectively. The two vertical dash lines show the region of the printable magnification rate. f) The influence of focal length and mask images on the printing resolution. The dashed lines show the printer's resolution using $f = 18mm$ objective lens. g) The influence of the magnification rate and the frustum angle on the printing velocity. The printable velocity for frustum angles of 10°, 20°, and 30° are marked in gray, red, and blue shaded, respectively. The dashed line is the maximum printing velocity of the continuous liquid interface production.

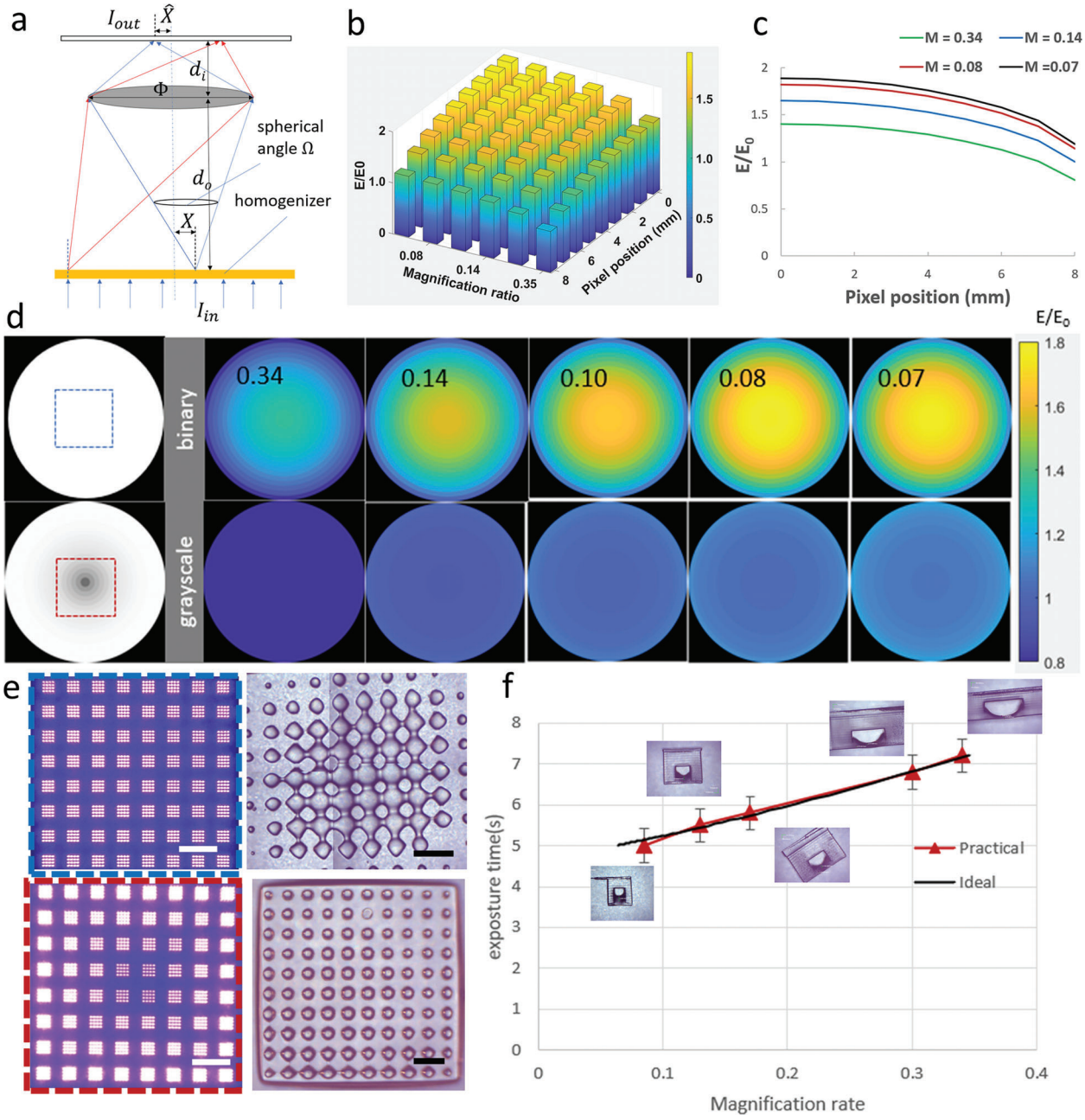

Figure 3. The models of light intensity distribution and light intensity compensation in zooming-focused MIP-VPP. a) The light path of zooming-focused MIP-VPP. b,c) The influence of pixel positions and the magnification rate on the light intensity. The magnification rate varies from 0.34 to 0.07. The pixel position varies from 0 to 8 mm to the optical center. d) The simulation of the grayscale light intensity compensation. The leftmost column of (d) shows the mask images applied to the LCD. The top row of (d) shows the relative energy dosage over magnification rate from 0.34 to 0.07 without grayscale compensation. The bottom row of (d) shows the relative energy dosage with grayscale compensation. e) The printing result of chessboard test cases to verify the light intensity compensation. Scale bars: 200 µm. The top row of (e) shows the physical mask image and the printing result without grayscale compensation. The bottom row of (e) shows the physical mask image and printing result with grayscale compensation. f) The printing result of test cases to verify the exposure time over different magnification rates. The black line shows the simulated exposure time over the magnification rates. The red line shows the practical exposure time over the magnification rate. The layer thickness is 76 µm.

square on the boundary, conforms to the simulation results. The grayscale compensation cancels out the non-uniformity of the light intensity, providing consistent printing results shown in Figure 3e-bottom. All squares in the printed results are similar in size, showing the uniform light intensity within a layer. However, as shown in Figure 3d-bottom, the relative energy dosage E/E_0 still changes as the magnification rate M decreases.

2) In the second step, the printing speed V_h is used to compensate for the light intensity change between different

magnification rates. That is, the printing speed V_h is increased when the magnification rate decreases and vice versa to get a constant relative energy dosage for a frustum layer. Figure 3f shows the exposure time to curing a layer with 76 μm layer thickness of Formlabs Clear resin at the magnification rate from 0.07 to 0.34. The black line is the predicted exposure time based on the compensation model. The red dots are the practical exposure time based on the calibration. The practical exposure time aligns well with the theoretical model, proving the feasibility of our light distribution model. In the continuous printing process, the desired exposure time can be converted into the pulling-up speed V_h of the building platform. Hence, light intensity uniformity can be achieved by controlling the grayscale mask pattern and the controlled pulling-up speed based on the developed light distribution model. A cone shape test case was printed with the two-step compensation strategy. A smooth surface with an accurate profile contour can be observed, demonstrating the capability of zooming-focused MIP-VPP for smooth and accurate surface fabrication. (Figure S2, Supporting Information)

We demonstrate the feasibility and performance of zooming-focused MIP-VPP by 3D printing customized optical lenses. Compound parabolic concentrator (CPC) elements have been widely used in solar energy systems.[42] They have the capability of reflecting all the incident light to the receivers at the entry aperture within the acceptance angle.[43] They are used as representative test cases in our study. **Figure 4**a,b illustrate the design of CPC elements. The total internal reflective (TIR) surface profile of the CPC elements is optimized to concentrate light energy to their receivers. The diameter of the receivers of the CPC elements is $d_2 = 1mm$ and the acceptance angle is $\alpha = 20°$, $30°\wedge 40°$. The 3D printing results of the CPC elements via zooming-focused MIP-VPP are demonstrated in Figure 4c. All the optical lenses were printed in a few minutes using a speed of around 11.2 μm s^{-1} (Table S4, Supporting Information). High transparency of light over the visible light spectrum can be observed from the printed samples without post-processing. The dimensional accuracy of the CPC elements with acceptance angles of 30° is measured from optical microscopy images, shown in Figure 4d,e. The radius of the designed CPC over the Z height is plotted as the black curve. And the mean radius of the printed CPC over the Z height is plotted in orange. The mean value of the surface profile matches well with the design value. The red dash line in Figure 4d shows the standard deviation of the surface profile. The standard deviation of less than 8 μm confirms good repeatability. Figure 4e shows the absolute error between the designed and printed radius over the Z height. The absolute deviation is well controlled within the range from −6.8 to 7.9 μm plotted in the functional region for light reflection. The deviation is mainly due to the light intensity distribution. The absolute deviation can be further reduced by better light intensity calibration. Beyond the functional region, the absolute deviation increases due to the material overcure at the base region. The scanning electron microscopy (SEM) images of the elements in Figure 4f reveal the smooth surface quality without stair-stepping typically associated with MIP-VPP. Figure 4f-right shows the 6500× magnified image of the surface close to the receiver. The smooth surface and sharp profile show excellent resolution. Furthermore, the surface roughness of the TIR surface measured via atomic force microscopy (AFM) is 3.4 nm within a 2 × 2 μm sampling region, quantified by the root mean square (R_{ms}) (Figure 4g). The maximum roughness depth R_{max} in the measured region is 8.0 nm.

The surface roughness result confirms that zooming-focused MIP-VPP is of high printing precision with the stair-stepping defect eliminated. Unlike previous studies relying on the meniscus coating process, the dimensional accuracy of the fabricated sample is explicitly defined by the zooming-focused MIP-VPP process, providing a controlled dimensional accuracy. We used light flux at the receiver to characterize the performance of the 3D-printed CPC samples concentrated on their outlets. Figure 4h shows the illumination performance over the varying incident angle. The lenses with acceptance angles equal to 20°, 30°, and 40° are noted in different colors. For the CPC elements with a $\alpha = 20°$, they have a light flux of 96k lux at the receiver of the devices when light is shooting at 0° incident angle. As a comparison, the light flux is 15k lux without CPC elements for the same area and incident angle. The CPC elements with $\alpha = 20°$ have a huge light flux drop as the incident light angle is larger than 20°. In comparison, the devices with $\alpha = 40°$ have a wider acceptance angle, showing a slower light flux change over the incident angle of the laser beam. The surface quality and dimensional accuracy of the 3D-printed samples are comparable to those made by conventional optics fabrication methods.[44] Therefore, zooming-focused MIP-VPP makes it possible to fabricate high-quality optical lenses rapidly.

To present the advantages of fabricating complex optical structures, we further demonstrate the capability of zooming-focused MIP-VPP in 3D-printing a fisheye lens and a laser beam expander consisting of multiple optical lenses.[45–47] **Figure 5**a shows the surface profile of a fisheye lens, in which the spherical lens is placed on a cylindrical base. The diameter of the fisheye lens is $r = 1.5mm$; the height of the cylinder base is $h_b = 0.5mm$; the curvature κ of the fisheye lenses varies from 0.63 to 0.4 mm^{-1} respectively. Figure 5b shows the optical microscopy images of the 3D-printed fisheye lens. The SEM image of its top surface shown in Figure 5c reveals smooth surfaces without visible stepping or pixelized aliasing under 230× magnification. Besides the nanoscale surface roughness, the dimensional accuracy of the fisheye lenses is studied. The fisheyes lenses with designed curvatures of 0.4, 0.5, 0.55, and 0.63 mm^{-1} were printed. Their fabrication time is around 2 min (Table S4, Supporting Information). The printed curvatures measured from optical images are 0. 413, 0.504, 0.549, and 0.632 mm^{-1}, ensuring dimensional fidelity, as displayed in Figure 5d. The lens with a smaller curvature has a larger error because, when the curvature is small, zooming-focused MIP-VPP requires a fast motion of the LCD and the objective lens, leading to larger errors. The optical performance of the printed fisheye lenses is measured in terms of lateral resolution. As shown in Figure 5e, the lateral resolution of the 3D-printed fisheye lens is characterized by imaging a USAF1951 resolution target at multiple illumination wavelengths. The multiple bandpass filters with center wavelengths of 441 nm, 635 nm, and white light were used for illumination. The aperture size of the imaging system is 3 mm. By imaging the resolution target using white light, the 3D-printed fisheye lenses can resolve the smallest feature in element 6 of group 7 (Figure 5f). Subsequently, the experimentally measured image modulation as a function of

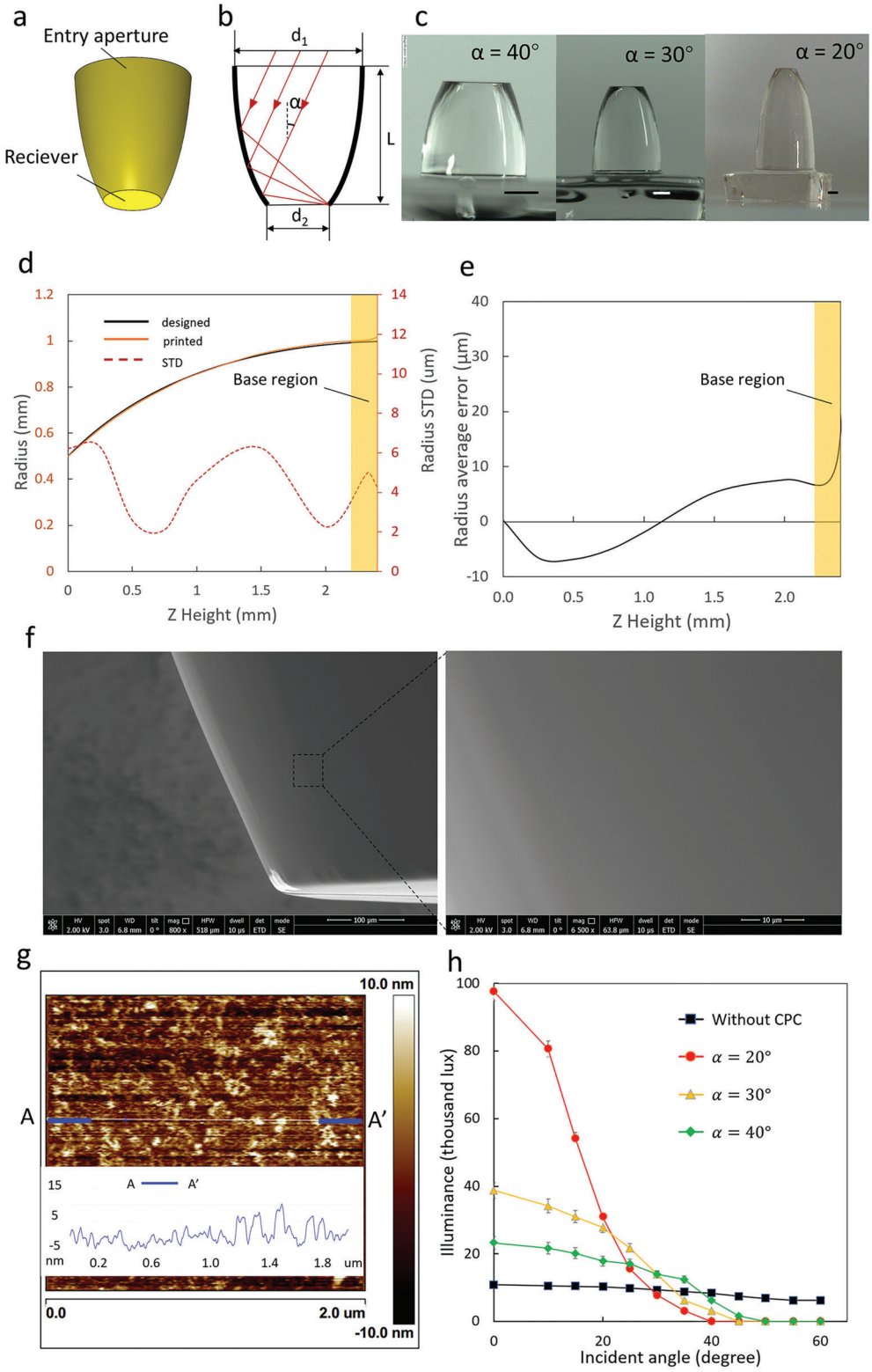

Figure 4. Customized CPC elements fabricated via zooming-focused MIP-VPP. a,b) Schematic illustration and design of CPC elements. c) Optical microscope images of the 3D-printed CPC elements with acceptance angles of 40°, 30°, and 20° (from left to right), scale bars: 500 μm. d) The surface profile of printed CPC elements. The black curve is the designed profile, and the orange curve is the printed profile. The standard deviation between samples is demonstrated in the red dash curve. e) The absolute deviation of radius over *Z* height between the designed and printed CPC elements. f) The SEM images of the 3D-printed CPC element at 800× and 6500× magnification. The left of (f) scale bars: 100 μm. The right of f) scale bars: 10 μm. g) The AFM images of the surface roughness of the CPC elements. h) The light collection performance of printed CPC elements over the acceptance angle, quantified by the illuminance at the receivers of the CPC elements.

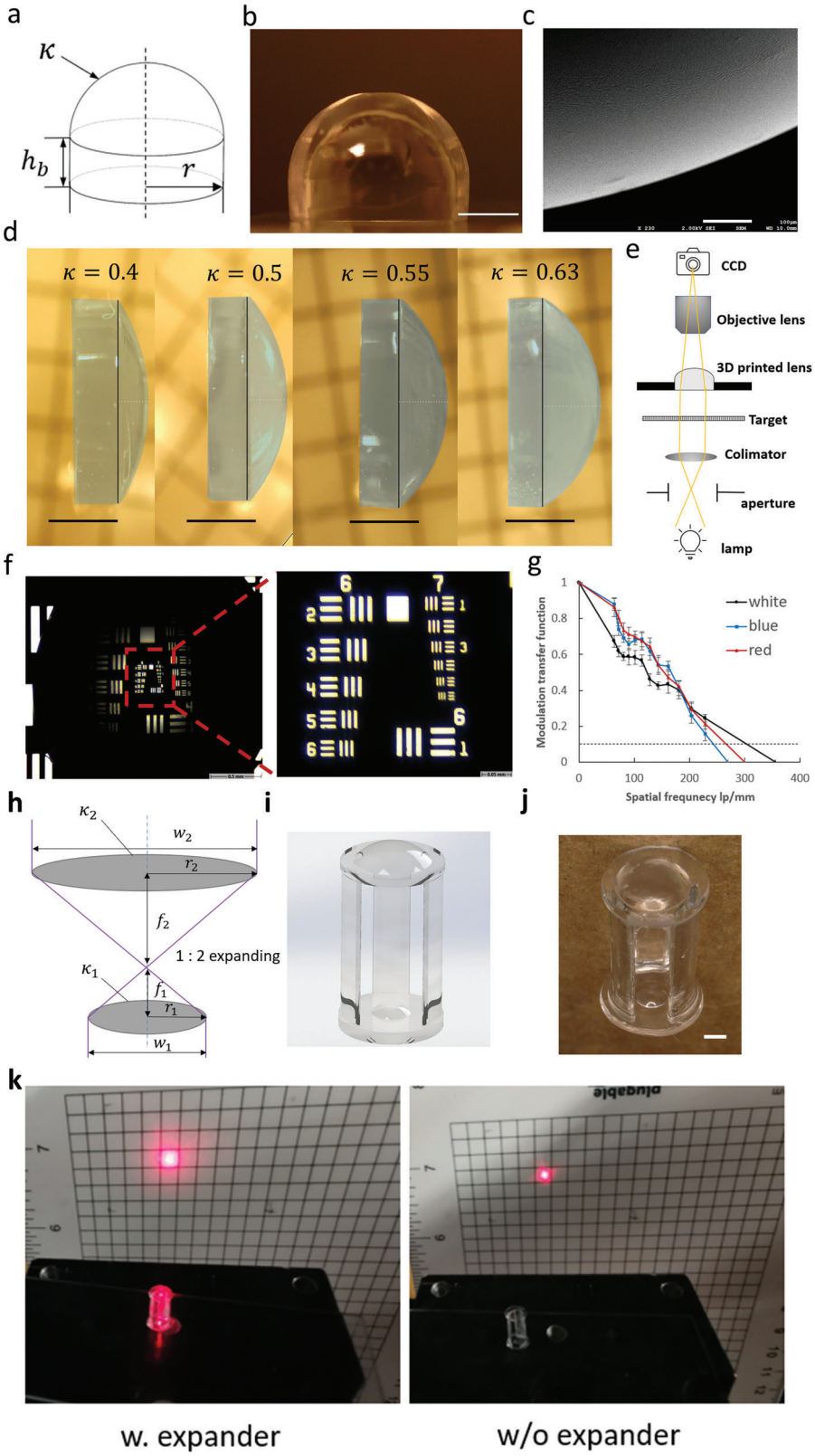

Figure 5. Fisheye lenses and laser beam expanders fabricated via zooming-focused MIP-VPP. a) Schematic design of the fisheye lens. b) Optical microscope image of the zooming-focused MIP-VPP printed fisheye lens, scale bar: 1 mm. c) SEM images of the zooming-focused MIP-VPP printed fisheye lens from the side view, scale bars: 100 µm. d) Optical microscope image of the zooming-focused MIP-VPP printed fisheye lens over different curvature, scale bar: 1 mm. e) Schematic illustration of the experimental setup to characterize the imaging resolution of the 3D-printed fisheye lens. f) Imaging

spatial frequency is calculated to define the modulation transfer function (MTF), Shown in Figure 5g. A 10% modulation of the MTF is used as a threshold to determine the imaging resolution. The MTF curves indicate the maximum imaging resolution at the spatial frequency of 244.8, 265.5, and 306.8 lp mm^{-1} under the illumination of blue, red, and white light, respectively.

A lens set is usually required for real-world applications. The position and orientation of multiple lenses in a lens set need to be accurately calibrated and positioned during assembly to minimize optical errors.[48,49] Here, we demonstrate the capability of zooming-focused MIP-VPP in directly fabricating an in-situ assembled lens set. A Keplerian laser beam expander is used as a representative example. Figure 5h shows the design of a 1:2 ratio laser beam expander. The focal lengths of the fisheye lenses are 2.17 and 4.35 mm, respectively. The CAD model of the laser beam expander is shown in Figure 5i. The 3D printed result, shown in Figure 5j, has two fisheye lenses with self-aligned optical centers. The two printed lenses offer accurate dimension control and smooth surface quality directly defined by the 3D-printing apparatus. (Figure S3, , Supporting Information) The first lens was directly printed on the building platform. Then the assembly features were printed using the traditional MIP-VPP process (V_l = 0). We used the in-situ transfer VPP[50] to add a flat base to the assembly features, on which the second lens was printed using zoom-focused MIP-VPP. The performance of the beam expander was studied by shooting a laser beam of 635 nm wavelength through it. The laser beam through the beam expander projects a larger round dot on a grid screen that is 100 mm away from the expander, as shown in Figure 5k-left, compared to the laser beam without expander shown in Figure 5k-right (refer to Video S1, Supporting Information). Therefore, 3D-printed optical devices with complex structures, including mechanical fixtures, could be fabricated in situ by zooming-focused MIP-VPP, which supports high surface smoothness and high dimensional accuracy printing for both lenses and assembly features.

3. Conclusion

A zooming-focused MIP-VPP-based 3D printing process has been presented for optical lens fabrication. The zooming-focused MIP-VPP uses frustum layer stacking to reduce the staircase stepping and improve the surface roughness so microscale dimensional accuracy and nanoscale surface roughness can be achieved. Consequently, no post-processing, such as meniscus coating and surface polishing, is needed. We demonstrated the capability of zooming-focused MIP-VPP in 3D printing CPC elements and fisheye lenses with subwavelength surface roughness (3.4 nm) and pixel scale dimensional accuracy (14.7 μm) within minutes, offering a low-cost solution for the rapid fabrication of customized optical lenses. We further demonstrate the printing of an in situ assembled beam expander with a 1:2 expanding ratio, offering the advantage of integrated optical device fabrication. The 3D-printed assembly enabled by zooming-focused MIP-VPP features high surface quality and remarkable positioning accuracy over each optical lens. Consequently, any assembly error or additional calibration effort during the lens assembly could be avoided.

With the principle of zooming-focused MIP-VPP demonstrated, its fabrication scale can be adjusted by enlarging or shrinking the sizes of the imaging system for lenses suitable for various engineering systems. The mask projection system can also be improved, such as better light intensity calibration, expanding the aperture size of the objective lens to provide a larger mask image on the building platform, and reducing pixel sizes.[51] The use of frustum layer stacking opens a new avenue for 3D printing optical components and other devices that require a high surface roughness and dimensional accuracy. While our current approach has been developed to effectively handle optical lenses with symmetric shapes, how to achieve frustum layer stacking for more complex lens designs such as Kinoform and the freeform lens remains an open research question.

4. Experimental Section

Inhouse-Developed Zooming-Focused MIP-VPP Printer: The hardware of the zooming-focused MIP-VPP prototype (Figure S1, Supporting Information) comprises a 72 W LED array with 405 nm irradiation wavelength (Mars 2 pro, ELEGOO, China), a light homogenizer (N-BK7 Ground Glass Diffusers 120grit, Thorlabs, US), a 1620 × 2560 resolution LCD photomask (Mars 2 pro, ELEGOO, China) with pixels size of 50 μm, and an objective lens (PLN 10×, Olympus, Japan), a liquid resin vat with oxygen inhibition coating (186 silicone elastomer 1:10 weight ratio, SYLGARD, UK), a glass plate of building platform are mounted under a mobile building platform (M-605, Physik Instrumente L.P., USA). The light intensity of the LED array is proportional to the pulse width modulation (PWM) value of the LED driver from 0 to 255. Two stepper-motorized linear stages (XS-LIDE, Velmex, USA) controlled the objective and imaging distance. The maximum travel distance of the objective lens was 24.5 mm, and the maximum travel distance of the LCD photomask was 380 mm. The projection area of the mask images was 5 × 5 mm. The maximum elevation speed of the building platform was 120 μm s^{-1}.

Layer Stacking Error: The layer stackings error shown in Figure 1e is quantified by metric error. The metric error ϵ_k of the k_{th} layer was defined as the integral of a metric profile function along that layer's height range $[z|k-1, z_k]$.

$$\epsilon_k = \int_{z_{k-1}}^{z_k} \varphi(z)\, dz \tag{5}$$

where $\varphi(z)$ can be written as the area deviation: $\varphi(z) = A(z) - A_0(z)$. A_0 is the designed area of the cross-section at height z, and A is the practical area of the cross-section at height z.

The magnification rates of the mask images in Figure 2e were taken by a pluggable USB digital microscope (USB2-MICRO-250X, Pluggable, China) at 250x magnification. The theoretical resolution of the changes of mask images in Figure 2f is calculated based on the following equation.

$$\mathrm{Re} = \frac{\delta d_i * D}{2f} \tag{6}$$

resolution of the printed fisheye lens measured by USAF 1951 resolution target, scale bar: 500 μm (left), scale bar: 50 μm (right). g) Experimentally measured MTF for the zooming-focused MIP-VPP printed lens at wavelength 441 nm (blue), 635 nm (red), and white light. h) Schematic illustration of the laser beam expander with a 1:2 expanding ratio. i) CAD model of the laser expander. j) Printing result of the 3D-printed laser expander, scale bar: 1 mm. k) Beam expanding performance of the 3D-printed laser beam expander.

where Re is the resolution, δd_i is the minimum steps of the linear stage, D is the mask image size, and f is the focal length of the objective lens.

The maximum printing speed $\hat{V}_h$ in Figure 2g is calculated based on the following equation.

$$\hat{V}_h = \frac{V_{lcd} M^2 D}{2f} tan(\theta) \tag{7}$$

where $\hat{V}_{lcd} = 22.8$ mm s^{-1} is the maximum moving speed of the LCD photomask.

Light Intensity Modeling and Compensation: The curing depth could be modelized based on the input UV dose and the curing threshold of the resin, governed by the equation.

$$C_d = D_p ln\left(\frac{I \cdot t}{E_c}\right) \tag{8}$$

where C_d is the curing depth of the resin, D_p is the penetration depth varying from materials, I is the light intensity, t is the exposure time, E is the absorbed energy dosage, and E_c represents a critical energy dosage.[52]

The light intensity distribution over the building platform was simulated by the numeric computing platform (MATLAB &Simulink, MathWorks, USA). The diffusing angles of the incoming light were provided by the bidirectional scattering distribution function. (N-BK7 ground glass diffusers 120grit, Thorlabs, USA) The diameter of the objective lens was measured from the physical lens using a caliper. The grayscale compensation was performed by the test case of 200 × 200 µm square chessboard. They were printed using 76 µm layer thickness for 8 s UV exposure. The test cases for the exposure time compensation study were 1 mm overhang beams. They were printed under 76 µm layer thickness. The thickness of the built overhanging beams was measured using a microscale inspection device (VH-S30B, Keyence, Japan).

Zooming-Focused MIP-VPP Printing Processes: A transparent commercial UV-curable resin (Eglass-2.0, EnvisionTEC, USA) was used to print all the test cases. The photocurable resin was shaken and defoamed by the planetary centrifugal mixer (THINKY MIXER AR-100, THINKY corporation Japan) for 5 and 3 min, respectively. The CAD model sliced with a thickness of 1.0 µm was printed continuously with a printing speed of ≈5–120 µm s^{-1}. The LED array was working at its maximum PWM value of 255. A 200 µm cylindrical based structure was printed at 5 µm s^{-1} to enhance the bounding between the optics and the building platform. After 3D printing, the residue resin was removed by a 30 s ultrasound bath in 99.5% isopropyl alcohol (IPA 99.5%, gotparts747, USA), followed by 30 s high-pressure nitrogen flushing. The structure was further UV cured for 15 min using a post-curing machine (Form Cure, Formlabs, USA) to cure the surface resin fully.

Design of the 3D-Printed CPC: The surface profile of the CPC (Figure 4b) was designed to achieve the designated acceptance angle α. The diameter of the bottom was governed by the equation $d_1 = \frac{d_2}{sin(\alpha)}$, the height of the elements was $h = \frac{d_1+d_2}{2tan(\alpha)}$. The theoretical optimal concentration of the CPC elements was given by $C_{max} = \frac{1}{sin^2(\alpha)}$.

Design of the 3D-Printed Fisheye and Laser Beam Expander: The profiles of the fisheye lenses (Figure 5h) were designed as spherical surfaces. The curvature radiuses of the fisheye lenses varied from 3.0 to 1.0 mm. The fisheye lenses' diameters ranged from 3.0 to 1.5 mm. The focal distance of the fisheye lenses was designed based on the equation $\frac{1}{\kappa} = (n-1)f$, where κ is the curvature, n is the reflective index of the cured resin, and f is the focal distance. The design of the laser beam expander is governed by the following equation.

$$M_e = \frac{f_2}{f_1} = \frac{r_2}{r_1} = \frac{h_2}{h_1} \tag{9}$$

Optical Performance Characterization of 3D-Printed Optics: The surface quality of the 3D-printed optics was studied using scanning electron microscopy (JSM-7001, JEOL, Japan) at an accelerating voltage of 2.0 kV and a spot size of 3.0. The surface roughness of 3D-printed CPC elements was characterized by atomic force microscopy (ICON SPM, Bruker, Germany) working in tapping mode with a PPP-NCHR probe (Nanosensors, Switzerland). The dimensional accuracy of the 3D-printed optics was studied through the stereo microscope (VH-S30B, Keyence, Japan). The light flux of the CPC elements was measured by a light flux meter (LT300, EXTECH, USAA), and the light source of the CPC elements was generated by a 635 nm laser source (ABP-N, LaserGlow Technologies, US). The MTF was measured by USAF 1951 standard resolution target (Thorlabs, USA) with a 10-group pattern from −2 to +7. The beam expander was verified by shooting a red laser from a 635 nm laser source (ABP-N, LaserGlow Technologies, US). A light screen with 5 mm grids (Plugable, China) collected the beam-expanding result.

Supporting Information

Supporting Information is available from the Wiley Online Library or from the author.

Acknowledgements

This work used AFM imaging provided by the Center of Excellence in NanoBiophysics at the University of Southern California. The authors acknowledge the support from National Science Foundation (NSF) (Grant Nos. CMMI 1151191, 1335476, and 1812675).

Conflict of Interest

The authors declare no conflict of interest.

Author Contributions

Y.C. developed the concept and supervised the project. H.X. designed the study and performed the experiments. H.X. performed the simulation of frustum layer stacking. H.X. performed the simulation of the light intensity distribution. M.H. performed a preliminary study. S.C. and R.H. fabricated test cases and experimentally characterized the dimensional accuracy. Y.Y. and H.X. performed imaging measurements. R.H. characterized the surface roughness. Y.X. characterized the optical performance of the samples. H.X, S.C., R.H., M.H., Y.X., Y.Y., and Y.C. prepared the manuscript. All authors discussed the results and contributed to the manuscript.

Data Availability Statement

The data that support the findings of this study are available in the supplementary material of this article.

Keywords

additive manufacturing, continuous printing, optical lens, slant angle, vat polymerization

Received: January 17, 2023
Revised: May 4, 2023
Published online:

[1] W. Gao, Y. Zhang, D. Ramanujan, K. Ramani, Y. Chen, C. B. Williams, C. C. L. Wang, Y. C. Shin, S. Zhang, P. D. Zavattieri, *Comput.–Aided Des.* **2015**, *69*, 65.

[2] J. W. Stansbury, M. J. Idacavage, *Dent. Mater.* **2016**, *32*, 54.
[3] K. J. Krieger, N. Bertollo, M. Dangol, J. T. Sheridan, M M. Lowery, E. D. O'cearbhaill, *Microsyst. Nanoeng.* **2019**, *5*, 42.
[4] Y. Xu, Z. Wang, S. Gong, Y. Chen, *Addit. Manuf.* **2021**, *39*, 101840.
[5] X. Song, Y. Pan, Y. Chen, *J. Manuf. Sci. Eng.* **2015**, *137*, 021005.
[6] X. Li, W. Shan, Y. Yang, D. Joralmon, Y. Zhu, Y. Chen, Y. Yuan, H. Xu, J. Rong, R. Dai, Q. Nian, Y. Chai, Y. Chen, *Adv. Funct. Mater.* **2021**, *31*, 2003725.
[7] H. Xu, S. Chen, F. Luo, H. Mao, Y. Chen, *J. Manuf. Processes* **2020**, *56*, 1322.
[8] X. Li, Y. Yuan, L. Liu, Y.-S. Leung, Y. Chen, Y. Guo, Y. Chai, Y. Chen, *Bio–Des. Manuf.* **2020**, *3*, 15.
[9] B. H. Cumpston, S. P. Ananthavel, S. Barlow, D. L. Dyer, J. E. Ehrlich, L. L. Erskine, A. A. Heikal, S. M. Kuebler, I.-Y. S. Lee, D. Mccord-Maughon, J. Qin, H. Röckel, M. Rumi, X.-L. Wu, S. R. Marder, J. W. Perry, *Nature* **1999**, *398*, 51.
[10] F. Kotz, A. S. Quick, P. Risch, T. Martin, T. Hoose, M. Thiel, D. Helmer, B. E. Rapp, *Adv. Mater.* **2021**, *33*, 2006341.
[11] R. Bogue, *Assem. Autom.* **2013**, *33*, 307.
[12] Y. Yang, X. Song, X. Li, Z. Chen, C. Zhou, Q. Zhou, Y. Chen, *Adv. Mater.* **2018**, *30*, 1706539.
[13] Y. Yang, X. Li, X. Zheng, Z. Chen, Q. Zhou, Y. Chen, *Adv. Mater.* **2018**, *30*, 1704912.
[14] R. Hai, G. Shao, C. Sun, in *Proc. SPIE 11292*, SPIE, San Francisco, CA **2020**, pp. 126–135.
[15] D. Gonzalez-Hernandez, S. Varapnickas, A. Bertoncini, C. Liberale, M. Malinauskas, *Adv. Opt. Mater.* **2023**, *11*, 2201701.
[16] D. Gonzalez-Hernandez, S. Varapnickas, G. Merkininkaitė, A. Čiburys, D. Gailevičius, S. Šakirzanovas, S. Juodkazis, M. Malinauskas, *Photonics* **2021**, *8*, 577.
[17] L. Jonušauskas, D. Gailevičius, S. Rekštytė, T. Baldacchini, S. Juodkazis, M. Malinauskas, *Opt. Express* **2019**, *27*, 15205.
[18] X. Li, T. Baldacchini, Y. Chen, *J. Micro Nano-Manuf.* **2021**, *9*, 041005.
[19] D. B. Gregory, S. T. Tomasz, *Opt. Express* **2019**, *27*, 30405.
[20] K. Willis, E. Brockmeyer, S. Hudson, I. Poupyrev, presented at Proc. of the 25th Annual ACM Symp. on User Interface Software and Technology, Cambridge, Massachusetts, USA, October **2012**.
[21] B. G. Assefa, M. Pekkarinen, H. Partanen, J. Biskop, J. Turunen, J. Saarinen, *Opt. Express* **2019**, *27*, 12630.
[22] M. J. Kim, H. T. Kim, J. K. Kang, D. H. Kim, D. H. Lee, S. H. Lee, S. H. Sohn, *Mol. Cryst. Liq. Cryst.* **2010**, *532*, 1..
[23] A. Larena, F. Millán, G. Pérez, G. Pinto, *Appl. Surf. Sci.* **2002**, *187*, 339.
[24] J. R. Tumbleston, D. Shirvanyants, N. Ermoshkin, R. Janusziewicz, A. R. Johnson, D. Kelly, K. Chen, R. Pinschmidt, J. P. Rolland, A. Ermoshkin, E. T. Samulski, J. M. Desimone, *Science* **2015**, *347*, 1349.
[25] X. Chen, W. Liu, B. Dong, J. Lee, H. O. T. Ware, H. F. Zhang, C. Sun, *Adv. Mater.* **2018**, *30*, 1705683.
[26] G. Shao, R. Hai, C. Sun, *Adv. Opt. Mater.* **2020**, *8*, 1901646.
[27] Y. Zhang, L. Wu, M. Zou, L. Zhang, Y. Song, *Adv. Mater.* **2022**, *34*, 2107249.
[28] C. Yuan, K. Kowsari, S. Panjwani, Z. Chen, D. Wang, B. Zhang, C. J.-X. Ng, P. V. Y. Alvarado, Q. Ge, *ACS Appl. Mater. Interfaces* **2019**, *11*, 40662.
[29] K. Kowsari, B. Zhang, S. Panjwani, Z. Chen, H. Hingorani, S. Akbari, N. X. Fang, Q. Ge, *Addit. Manuf.* **2018**, *24*, 627.
[30] Y. Pan, Y. Chen, *J. Micro Nano-Manuf.* **2015**, *3*, 031001.
[31] Y. Pan, Y. Chen, *Addit. Manuf.* **2016**, *12*, 321.
[32] Y. Pan, X. Zhao, C. Zhou, Y. Chen, *J. Manuf. Processes* **2012**, *14*, 460.
[33] H. Mao, T.-H. Kwok, Y. Chen, C. C. L. Wang, *Comput.–Aided Des.* **2019**, *107*, 89.
[34] C. Zhou, Y. Chen, Z. Yang, B. Khoshnevis, *Rapid Prototyping J.* **2013**.
[35] Y. Yang, Z. Wang, Q. He, X. Li, G. Lu, L. Jiang, Y. Zeng, B. Bethers, J. Jin, S. Lin, S. Xiao, Y. Zhu, X. Wu, W. Xu, Q. Wang, Y. Chen, *Research* **2022**, *2022*, 9840574.
[36] D. Dendukuri, P. Panda, R. Haghgooie, J. M. Kim, T. A Hatton, P. S. Doyle, *Macromolecules* **2008**, *41*, 8547.
[37] Y. Pan, C. Zhou, Y. Chen, *J. Manuf. Sci. Eng.* **2012**, *134*, 051011.
[38] X. Li, H. Mao, Y. Pan, Y. Chen, *J. Manuf. Sci. Eng.* **2019**, *141*, 081007.
[39] C. Xia, N. Fang, *J. Micromech. Microeng.* **2009**, *19*, 115029.
[40] C. Zhou, H. Xu, Y. Chen, *Adv. Intell. Syst.* **2021**, *3*, 2100079.
[41] X. Zheng, J. Deotte, M. P. Alonso, G. R. Farquar, T. H. Weisgraber, S. Gemberling, H. Lee, N. Fang, C. M. Spadaccini, *Rev. Sci. Instrum.* **2012**, *83*, 125001.
[42] F. Ullah, M. K. Khattak, K. Min, *Energy Environ.* **2018**, *29*, 770.
[43] S. A. Kalogirou, in *Solar Energy Engineering: Processes and Systems*, 10th ed., Academic Press, Cambridge, Massachusetts, USA **2013**.
[44] H.-J. Choi, C. Cho, S. Woo, J.-Y. Lee, Y.-E. Yoo, M. Jeon, G.-H. Kim, T.-J. Je, E.-C. Jeon, *Int. J. Precis. Eng. Manuf.–Green Technol.* **2021**, *8*, 1405.
[45] S. Nayar, S. Bhuminathan, W. Bhat, *J. Pharm. BioAllied Sci.* **2015**, *7*, 216.
[46] F. Duerr, H. Thienpont, *Opt. Express* **2015**, *23*, 30438.
[47] W. S. Jagger, *Vision Res.* **1992**, *32*, 1271.
[48] I. A. Levin, Y. Y. Kachurin, *J. Opt. Technol.* **2021**, *88*, 178.
[49] R. M. Malone, B. C. Cox, V. E. Fatherley, B. C. Frogget, G. P. Grim, M. I. Kaufman, K. D. McGillivray, J. A. Oertel, M. J. Palagi, W. M. Skarda, A. Tibbitts, C. H. Wilde, M. D. Wilke, in *Proc. SPIE 7793*, SPIE, San Diego, CA **2010**, pp. 107–121.
[50] Y. Xu, F. Qi, H. Mao, S. Li, Y. Zhu, J. Gong, L. Wang, N. Malmstadt, Y. Chen, *Nat. Commun.* **2022**, *13*, 918.
[51] P. S. Nair, H. Wang, J. Trisno, Q. Ruan, S. D. Rezaei, R. E. Simpson, J. K. W. Yang, *ACS Photonics* **2022**, *9*, 2024.
[52] D. F. Swinehart, *J. Chem. Educ.* **1962**, *39*, 333.